

Phase Modeling of the TRAPPIST-1 Planetary Atmospheres

STEPHEN R. KANE,¹ TIFFANY JANSEN,² THOMAS FAUCHEZ,³ FRANCK SELSIS,⁴ AND ALMA Y. CEJA¹

¹*Department of Earth and Planetary Sciences, University of California, Riverside, CA 92521, USA*

²*Department of Astronomy, Columbia University, New York, NY 10027, USA*

³*NASA Goddard Space Flight Center, Greenbelt, MD 20771, USA*

⁴*Laboratoire d'astrophysique de Bordeaux, Univ. Bordeaux, CNRS, B18N, allée Geoffroy Saint-Hilaire, 33615 Pessac, France*

ABSTRACT

Transiting compact multi-planet systems provide many unique opportunities to characterize the planets, including studies of size distributions, mean densities, orbital dynamics, and atmospheric compositions. The relatively short orbital periods in these systems ensure that events requiring specific orbital locations of the planets (such as primary transit and secondary eclipse points) occur with high frequency. The orbital motion and associated phase variations of the planets provide a means to constrain the atmospheric compositions through measurement of their albedos. Here we describe the expected phase variations of the TRAPPIST-1 system and times of superior conjunction when the summation of phase effects produce maximum amplitudes. We also describe the infrared flux emitted by the TRAPPIST-1 planets and the influence on the overall phase amplitudes. We further present the results from using the global circulation model ROCKE-3D to model the atmospheres of TRAPPIST-1e and TRAPPIST-1f assuming modern Earth and Archean atmospheric compositions. These simulations are used to calculate predicted phase curves for both reflected light and thermal emission components. We discuss the detectability of these signatures and the future prospects for similar studies of phase variations for relatively faint M stars.

Keywords: planetary systems – techniques: photometric – stars: individual (TRAPPIST-1)

1. INTRODUCTION

The phase variations of an exoplanet are caused by the observed reflected light and thermal emission components of an exoplanet as it orbits the host star. Reflected phase signatures can reveal the albedo and scattering properties of planetary atmospheres and thus provide a unique insight into their compositions, while thermal signatures can reveal the efficiency of heat transport from the dayside to the nightside. Though small in amplitude compared with the flux of the star, the cyclic nature of the phase variations allow them to be detected given a long enough temporal baseline of observations. In particular, precision photometry from the *Kepler* mission has demonstrated that phase signatures of orbiting exoplanets are indeed present and detectable in the data (e.g., Esteves et al. 2013, 2015; Quintana et al. 2013; Angerhausen et al. 2015). Such phase investigations are continuing in the era of the Transiting Exoplanet Sur-

vey Satellite (*TESS*), with phase signatures detected for numerous known exoplanets (e.g., Shporer et al. 2019; Jansen & Kipping 2020; Wong et al. 2020).

The recent discovery of the TRAPPIST-1 planetary system presents an interesting opportunity to study how atmospheric reflectivity and heat transport can affect the photometric observations. The system was initially detected by Gillon et al. (2016) and found to harbor three terrestrial transiting planets. Continued monitoring of the system with ground and space-based observatories revealed that the system has four additional terrestrial transiting planets (Gillon et al. 2017), three of which are within the Habitable Zone (HZ) of the host star (Bolmont et al. 2017), with planet e having the most potentially favorable conditions for surface liquid water (Wolf 2017). Analysis of the Transit Timing Variations (TTVs) by Grimm et al. (2018) produced improved mass and density estimates, constraining the interior models and fractions of volatiles. A lack of absorption features from Hubble Space Telescope (HST) observations during transit excludes cloud-free hydrogen-dominated at-

mospheres for most of the planets, leaving open the potential for temperate surface conditions (de Wit et al. 2018; Ducrot et al. 2018; Zhang et al. 2018). Even so, the activity of the host star and high XUV irradiation of the planets may have had a profound effect on their atmospheres (Becker et al. 2020; Peacock et al. 2019; Fleming et al. 2020), possibly leading to substantial loss of their atmospheric mass (Roettenbacher & Kane 2017; Wheatley et al. 2017; Hori & Ogihara 2020). Further observations by the *K2* mission enabled the confirmation of the outer planet and verification of its orbital period (Luger et al. 2017b). A compilation of transit data by Agol et al. (2020) further refined the planetary masses to a precision of 3–5%. The orbital architecture of this compact planetary system ensures that there are relatively frequent “syzygy” events, such as planet-planet occultations (Luger et al. 2017a), and occasions when multiple planets simultaneously contribute to the maximum reflected light at superior conjunction. Such events will allow tests of atmospheric models to be conducted based on the amplitude of the phase signatures and the passbands at which they are observed.

In this paper we model the phase variations of the TRAPPIST-1 system and the connection to models of the planetary atmospheres. In Section 2 we summarize the theoretical methodology to derive the photometric phase variations. In Section 3 we calculate the phase variations of the TRAPPIST-1 planetary system and predict maximum phase amplitudes for the individual planets and combined phase events for various geometric albedo assumptions. The phase variations resulting from global circulation models (GCM) of TRAPPIST-1e and TRAPPIST-1f are described in Section 4, including short-wave reflected light and long-wave thermal emission components. Section 5 contains a discussion of detectability prospects using current and future facilities, and the importance of distinguishing between different atmospheric evolution scenarios. Finally, we provide a summary of our work and concluding remarks in Section 6.

2. PHOTOMETRIC PHASE VARIATIONS

Photometry of exoplanet host stars with sufficient photometric precision and observational cadence can reveal the phase variations due to the planets (Shporer 2017) and can distinguish between planetary and stellar companions (Kane & Gelino 2012). Here we describe the variations at optical wavelengths due to the reflected and scattered light components of the photons received from the planet. Due to the relatively low mass of the planets in the TRAPPIST-1 system, the Doppler beam-

ing and ellipsoidal variation components have a negligible effect and are discussed in Section 5.

Here we adopt the formalism of Kane & Gelino (2010, 2011). The flux ratio of a planet with radius R_p to the host star at wavelength λ and phase angle α is given by

$$\epsilon(\alpha, \lambda) \equiv \frac{f_p(\alpha, \lambda)}{f_\star(\lambda)} = A_g(\lambda)g(\alpha, \lambda)\frac{R_p^2}{r^2} \quad (1)$$

where $A_g(\lambda)$ is the geometric albedo and $g(\alpha, \lambda)$ is the phase function. The star–planet separation, r , is given by

$$r = \frac{a(1 - e^2)}{1 + e \cos f} \quad (2)$$

where a is the semi-major axis, e is the orbital eccentricity, and f is the true anomaly. The phase angle, defined to be zero when the planet is at superior conjunction, is given by

$$\cos \alpha = -\sin(\omega + f) \quad (3)$$

The phase function $g(\alpha, \lambda)$ is often approximated by a Lambert sphere, which assumes the atmosphere isotropically scatters over 2π steradians. Here we adopt the empirically derived “Hilton function” (Hilton 1992), based upon observations of Jupiter and Venus and represented as a visual magnitude correction of the form

$$\Delta m(\alpha) = 0.09(\alpha/100^\circ) + 2.39(\alpha/100^\circ)^2 - 0.65(\alpha/100^\circ)^3 \quad (4)$$

resulting in a phase function of the form

$$g(\alpha) = 10^{-0.4\Delta m(\alpha)} \quad (5)$$

One of the main measurables from the detection of phase variations is the geometric albedo $A_g(\lambda)$, which in turn depends upon the surface conditions of the planet. Since many of the planets in the TRAPPIST-1 system are terrestrial and complete atmospheric desiccation may have occurred, there are various possible surface scenarios. For example, Kane et al. (2011) describe the three basic scenarios of rock, molten, and atmosphere in the context of 55 Cancri e, where rock and molten correspond to geometric albedos of 0.1 and 0.6 respectively. Given the equilibrium temperatures of the TRAPPIST-1 planets (Gillon et al. 2017), they are unlikely to have molten surfaces, but we adopt a “reflective” surface/atmosphere to represent the high geometric albedo of 0.6. Geometric albedos for planets with atmospheres vary enormously, depending on composition, cloud decks, haze layers, etc (Jansen & Kipping 2018; Madden & Kaltenecker 2018; Mansfield et al. 2019). For the atmosphere scenario, we adopt an Earth geometric albedo of 0.434, particularly as it lies in between the bare rock and reflective surface scenarios described above.

3. COMBINED PHASE AMPLITUDE

As noted in Section 1, the TRAPPIST-1 system is a particularly interesting science case, partly due to the compact nature of the system resulting in a high frequency of full orbital phases for each of the planets. Such a system poses a modeling challenge since the phase variations for all planets must be accounted for (Kane & Gelino 2013), but can also be an advantage if the planets regularly line up near superior conjunction where their phase amplitudes combine for a stronger effect (Gelino & Kane 2014). This is especially true for the TRAPPIST-1 system since the planets are close to orbital resonance (Gillon et al. 2017), ensuring regular occurrence of such superposition of phase effects.

The properties of the TRAPPIST-1 planets that are relevant to phase variations are shown in Table 1 (Gillon et al. 2017; Luger et al. 2017b). All seven planets are within 0.06 AU of the host star, with orbital periods all less than 20 days. The sizes of the planets indicate that all of them are in the terrestrial regime and, as mentioned in Section 1, three of the planets lie within the conservative HZ and an additional planet lies within the optimistic HZ (see Kane et al. (2016) for definitions of conservative and optimistic HZ boundaries). A study of the effect of revised stellar distances by Kane (2018) found that the TRAPPIST-1 planet semi-major axes and radii are relatively unaffected by the *Gaia* DR2 release (Gaia Collaboration et al. 2018).

We use the methodology described in Section 2 to construct a predicted phase amplitude model as a function of time for the system. As noted in Section 2, one of the primary components in the model is the geometric albedo for the planets. The phase amplitude for the three scenarios of rocky, reflective, and atmosphere (see Section 2) are shown in Table 1, along with a "maximum" amplitude calculated for an albedo of unity. These calculations include only the reflected light component integrated over a broad (bolometric) passband. The combined phase variation model using the unity albedos is represented in Figure 1, where the solid lines show the flux ratio for the individual planets and the dotted line shows the combined effect from all planets. The top panel depicts the phase variations for one complete orbit of the outer planet (h), and the bottom panel shows these same variations on the scale of an orbit of a HZ planet (e). As described by Kane & Gelino (2013), an accurate orbital ephemeris may be used to predict times when the combined effect of all planets will produce a relatively high phase amplitude.

An important component of exoplanet phase variations is that contributed by the infrared (IR) flux from the planet (Selsis et al. 2011). Using the calcu-

lated planetary equilibrium temperatures provided by Gillon et al. (2017), we estimated the IR flux from each of the planets that contribute to the passband of various instruments. Even the hottest of the planets, TRAPPIST-1b with a temperature of ~ 400 K, does not contribute significantly to the integrated flux for *Kepler* or *TESS* passbands. However, the eclipse depth will produce a stronger signature than that from phase variations and will depend on the wavelength at which it was observed. Shown in Figure 2 are the predicted eclipse depths for each of the seven known TRAPPIST-1 planets as a function of wavelength. These were calculated by integrating high resolution spectra for the star and planet into 0.15 micron bins (Baraffe et al. 2015). The top and bottom panels assume extreme values for the planetary albedos of 0.1 and 0.9, respectively. The models also assume local Lambertian scattering for the reflected flux and local radiative equilibrium for the thermal emission. As expected, the high atmospheric absorption scenarios produce the most detectable features at longer wavelengths. The IR signatures of the planets are explored in the context of the GCM results provided in Section 4.

4. ROCKE-3D GCM PHASE CURVES

4.1. Description of the Model

We have employed the Resolving Orbital and Climate Keys of Earth and Extraterrestrial Environments with Dynamics (ROCKE-3D) GCM (Way et al. 2017) to simulate TRAPPIST-1e and TRAPPIST-1f (Gillon et al. 2017) atmospheric circulation using the updated planet parameters from Grimm et al. (2018) assuming a synchronous rotation and aqua-planet configuration. The stellar spectrum of TRAPPIST-1 is represented by a 2600 K BT Settl with $[\text{Fe}/\text{H}] = 0$ (Baraffe et al. 2015). ROCKE-3D was run at a $4^\circ \times 5^\circ$ (46×72 coordinates) latitude-longitude resolution with an altitude resolution of 40 layers up to 0.1 mb.

For TRAPPIST-1e, we have simulated both a 1 bar modern Earth-like atmosphere mostly composed of N_2 and 400 ppm of CO_2 , and a 1 bar Archean-like atmosphere composed of N_2 , 10,000 ppm of CO_2 and 2,000 ppm of CH_4 such as assumed in composition B of Charnay et al. (2013). For TRAPPIST-1f, the modern Earth atmospheric composition led to a fully frozen ocean from top to bottom and to the crash of the simulation. As a result, only the Archean Earth simulation from Charnay et al. (2013) was simulated for TRAPPIST-1f. Note that H_2O is treated as a variable specie, predicted by the GCM.

Table 1. TRAPPIST-1 planetary orbital parameters and flux ratios

Planet	P (days)	a (AU)	R_p (R_\oplus)	i (deg)	Flux Ratio (ppm)			
					Maximum	Rocky	Reflective	Atmosphere
b	1.5109	0.011	1.086	89.65	17.317	1.732	10.390	7.516
c	2.4218	0.015	1.056	89.67	8.729	0.873	5.237	3.788
d	4.0496	0.021	0.772	89.75	2.351	0.235	1.410	1.020
e	6.0996	0.028	0.918	89.86	1.925	0.193	1.155	0.835
f	9.2067	0.037	1.045	89.68	1.441	0.144	0.864	0.625
g	12.353	0.045	1.127	89.71	1.132	0.113	0.679	0.491
h	18.764	0.060	0.715	89.80	0.261	0.026	0.157	0.113

NOTE—Planetary properties extracted from [Gillon et al. \(2017\)](#) and [Luger et al. \(2017b\)](#).

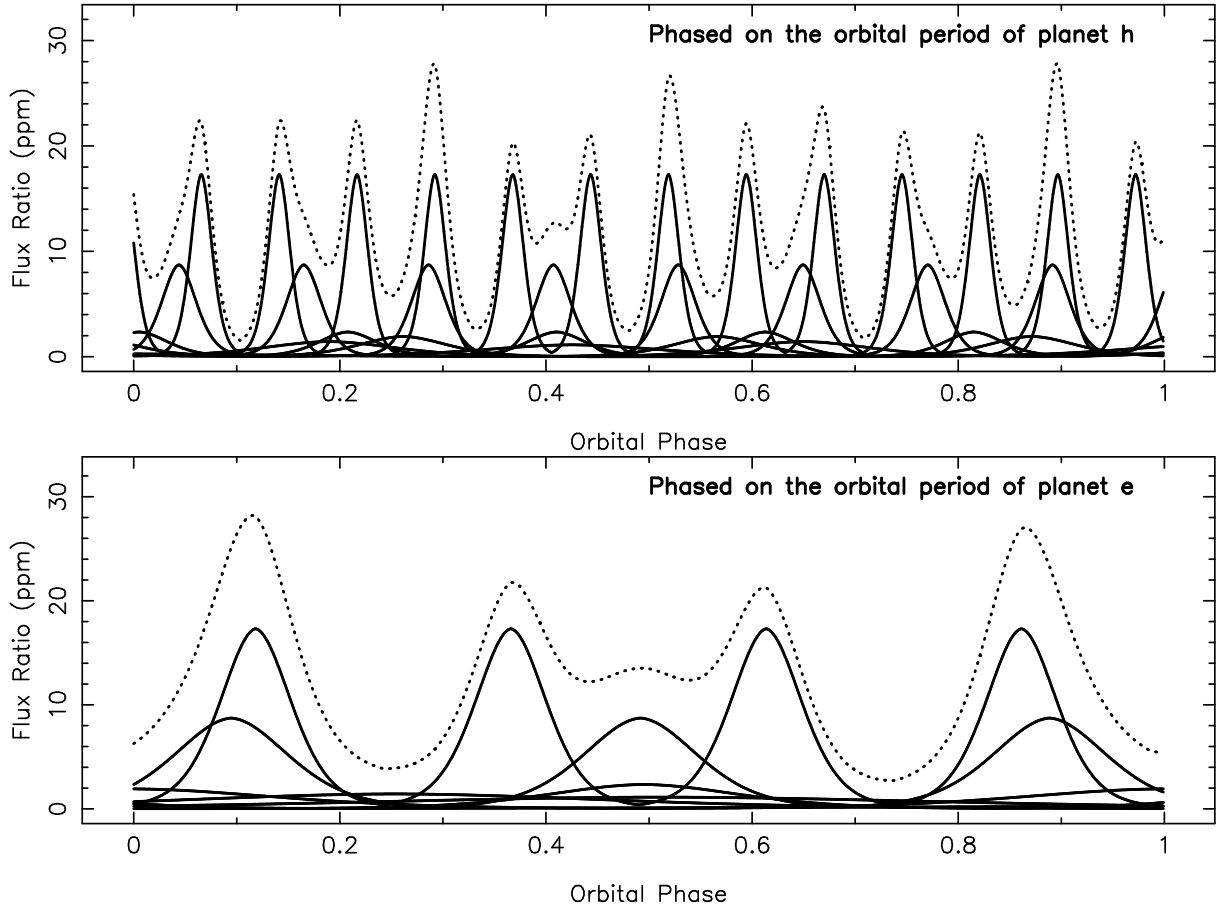


Figure 1. The combined flux variations of the TRAPPIST-1 system due to the reflected light from the planetary surfaces as a function of orbital phase. Individual planetary phase variations are shown as solid lines and the combined signature for all planets is shown as a dotted line. These calculations assume planetary albedos of unity so that the amplitudes may be scaled linearly to lower albedos. The top panel shows the phase variations for one complete orbit of the outermost planet, and the bottom panel is phased on the orbital period of planet e.

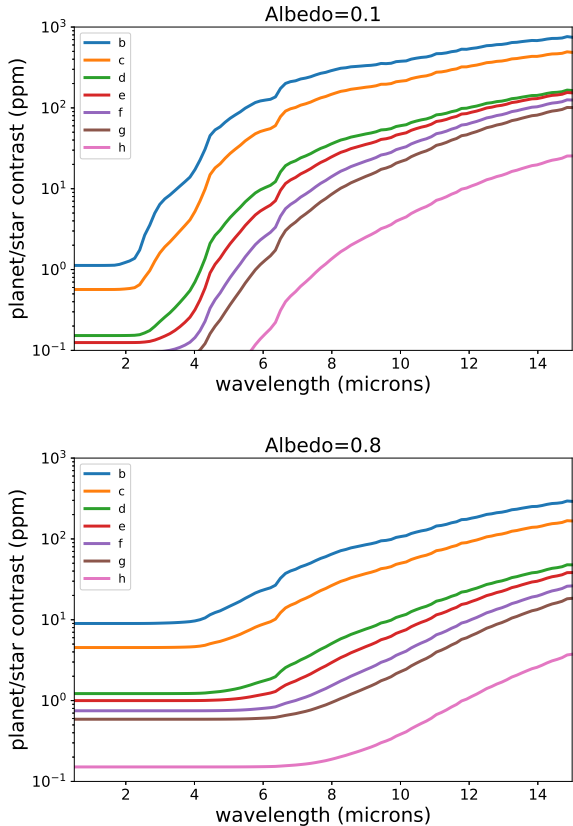


Figure 2. Predicted eclipse depth for the known TRAPPIST-1 planets as a function of wavelength, assuming an albedo of 0.1 (top panel) and 0.8 (bottom panel).

We used SOCRATES¹ radiation parameterization (Edwards & Slingo 1996; Edwards 1996) to compute the radiative transfer through the atmosphere as described by Way et al. (2017). For the modern Earth-like atmosphere, twelve bands in the longwave and twenty-one bands in the shortwave have been used to build the GCM, while twelve bands in the longwave and twenty-nine bands in the shortwave have been used in the case of the Archean Earth-like atmosphere (see Table 2 for the specific wavebands). These spectral resolutions lead to fluxes accurate to within several W/m² for planets orbiting an M dwarf such as TRAPPIST-1. TRAPPIST-1e is assumed to be fully covered by a global ocean (Unterborn et al. 2018) with a horizontal resolution 4° × 5° and 13 vertical layers down to a 100 m depth. The ocean includes ocean heat transport (OHT) with dynamic sea ice parameterization (Way et al. 2017) allowing fractional gridbox sea ice cover. The simula-

¹ <https://code.metoffice.gov.uk/trac/socrates>

Table 2. ROCKE-3D bandpasses (μm)

	modern Earth-like	Archean Earth-like
Short-wave	0.200 - 0.320	0.200 - 0.385
	0.320 - 5.050	0.385 - 0.500
	0.505 - 0.690	0.500 - 0.690
	0.690 - 0.770	0.690 - 0.870
	0.770 - 0.890	0.870 - 0.900
	0.890 - 0.980	0.900 - 1.080
	0.980 - 1.040	1.080 - 1.120
	1.040 - 1.100	1.120 - 1.160
	1.100 - 1.160	1.160 - 1.200
	1.160 - 1.240	1.200 - 1.300
	1.240 - 1.340	1.300 - 1.340
	1.340 - 1.420	1.340 - 1.420
	1.420 - 1.520	1.420 - 1.460
	1.520 - 1.620	1.460 - 1.520
	1.620 - 1.800	1.520 - 1.560
	1.800 - 1.960	1.560 - 1.620
	1.960 - 2.380	1.620 - 1.680
	2.380 - 2.950	1.680 - 1.800
	2.950 - 4.100	1.800 - 1.940
	4.100 - 4.500	1.940 - 2.000
4.500 - 20.00	2.000 - 2.140	
-	2.140 - 2.500	
-	2.500 - 2.650	
-	2.650 - 2.850	
-	2.850 - 3.150	
-	3.150 - 3.600	
-	3.600 - 4.100	
-	4.100 - 4.600	
-	4.600 - 20.00	
Long-wave	3.333 - 4.950	3.339 - 4.149
	4.950 - 6.667	4.149 - 4.566
	6.667 - 7.519	4.566 - 7.092
	7.519 - 8.130	7.092 - 7.634
	8.130 - 8.929	7.634 - 8.333
	8.929 - 10.10	8.333 - 8.929
	10.10 - 12.50	8.929 - 10.10
	12.50 - 13.33	10.10 - 12.50
	13.33 - 16.95	13.33 - 16.95
	16.95 - 18.18	12.50 - 18.18
	18.18 - 25.00	18.18 - 25.00
	25.00 - 10.00 × 10 ³	25.00 - 10.00 × 10 ³

tions were run until the radiative balance at the top of the atmosphere (TOA) was reached (e.g., a radiative imbalance smaller than ±0.2 Wm⁻²).

4.2. Constructing the Phase Curve

The ROCKE-3D phase curves of the TRAPPIST-1 planets are modeled as a sum of the outgoing short-wave radiation - a product of the incident stellar radiation and planetary albedo - and the outgoing long-wave thermal radiation across the longitudes which are visible to the observer at each point in phase. These radiation quantities are delivered by ROCKE-3D in static 2-dimensional grids spanning latitude and longitude, having been averaged over 100 model years post hydrological and radiative equilibrium. In order to represent the photometric phase variations of the modeled TRAPPIST-1 system from the perspective of an observer, we employ a moving window over the modeled surface that integrates over the observable longitudes as a function of phase and the given orbital dynamics, as described in the remainder of this section. The angle definitions and nomenclature in the following have been adapted from [Hu et al. \(2015\)](#).

For a phase angle α defined such that $\alpha = 0$ at occultation and $\alpha = \pm\pi$ at transit, the luminosity of the hemisphere viewed by an observer as a function of phase can be expressed simply as

$$L(\alpha) = L_{SW}(\alpha) + L_{LW}(\alpha). \quad (6)$$

Expanding the short-wave (SW) reflection component of the phase curve gives

$$L_{SW}(\alpha) = \sum_{\phi=\phi_i(\alpha)}^{\phi_j(\alpha)} \sum_{\theta=-\frac{\pi}{2}}^{\frac{\pi}{2}} [A_B(\xi(\phi), \theta) I(\xi(\phi), \theta) \times \mathcal{A}(\xi(\phi), \theta) \cos \theta \cos \phi], \quad (7)$$

where $A_B(\xi(\phi), \theta)$ is the Bond albedo of a specific grid cell, and $I(\xi(\phi), \theta)$ is the incident stellar radiation at the top of the atmosphere at the same grid cell, where each grid cell is defined by its latitude θ and local longitude ξ (which itself depends on the longitude in the observer's frame ϕ - more on this later). The outgoing short-wave radiation is then weighted by the grid cell area $\mathcal{A}(\xi(\phi), \theta)$ and the angle of its normal to the observer.

Adopting an inclination of 90° , the range of visible latitudes is constant with phase and defined to exist in $[-\pi/2, \pi/2]$ from the south pole to the north pole respectively. The planetary longitude in the observer's frame is defined such that $\phi = -\pi/2$ at the west terminator, $\phi = \pi/2$ at the east terminator, and $\phi = 0$ in the direction of the observer.

For the reflection component of the phase curve, the relevant range of longitudes $[\phi_i, \phi_j]$ is that which appears illuminated at a given phase. The western-most illuminated longitude ϕ_i and eastern-most illuminated longitude ϕ_j in the frame of the observer can be de-

scribed as a function of phase as

$$\phi_x(\alpha) = \begin{cases} \gamma\alpha - \pi/2 & x = i \\ -(\gamma - 1)\alpha + \pi/2 & x = j \end{cases} \quad (8)$$

where

$$\gamma = \begin{cases} 0 & -\pi < \alpha \leq 0 \\ 1 & 0 \leq \alpha < \pi \end{cases}.$$

These longitudes are then translated to the corresponding columns of the GCM grid (i.e. the "local longitudes" in the planetary frame, for which we use the symbol ξ) by considering the local longitude facing the observer at observation start, the planet's rotation frequency and orbital period, and the phase angles elapsed over the observation:

$$\xi(\phi_x, \alpha) = \phi_x(\alpha) + \xi_\delta(\alpha), \quad (9)$$

where ξ_δ is the local longitude in the direction of the observer at a given phase. For a planet on a prograde orbit, this is equal to

$$\xi_\delta(\alpha) = [\xi_0 - P f_{\text{rot}}(\alpha - \alpha_0)] \pmod{2\pi} \quad (10)$$

where α_0 is the phase angle at the start of the observation, ξ_0 is the local longitude in the direction of the observer at the start of the observation, P is the orbital period in days, and f_{rot} is the rotation frequency of the planet in days⁻¹. Assuming a synchronously rotating planet, as we do for TRAPPIST-1e and f, $P f_{\text{rot}} = 1$.

The long-wave component of the phase curve extracted from ROCKE-3D at a given phase angle can be similarly expressed as

$$L_{LW}(\alpha) = \sum_{\phi=-\frac{\pi}{2}}^{\frac{\pi}{2}} \sum_{\theta=-\frac{\pi}{2}}^{\frac{\pi}{2}} [F_T(\xi(\phi), \theta) \times \mathcal{A}(\xi(\phi), \theta) \cos \theta \cos \phi] \quad (11)$$

where $F_T(\xi(\phi), \theta)$ is the outgoing net thermal flux at the top of the atmosphere at a specific grid cell. Because the entire surface emits long-wave radiation throughout its orbit, the western and eastern-most radiating longitudes in the frame of the observer are constant in phase for the thermal component of the phase curve. Translating these longitudes to the local longitudes can then be done using Equation 9, redefining the first term ϕ_x as

$$\phi_x = \begin{cases} -\pi/2 & x = i \\ \pi/2 & x = j \end{cases}. \quad (12)$$

Because the model data are given in a relatively low resolution of latitude and longitude, the longitude

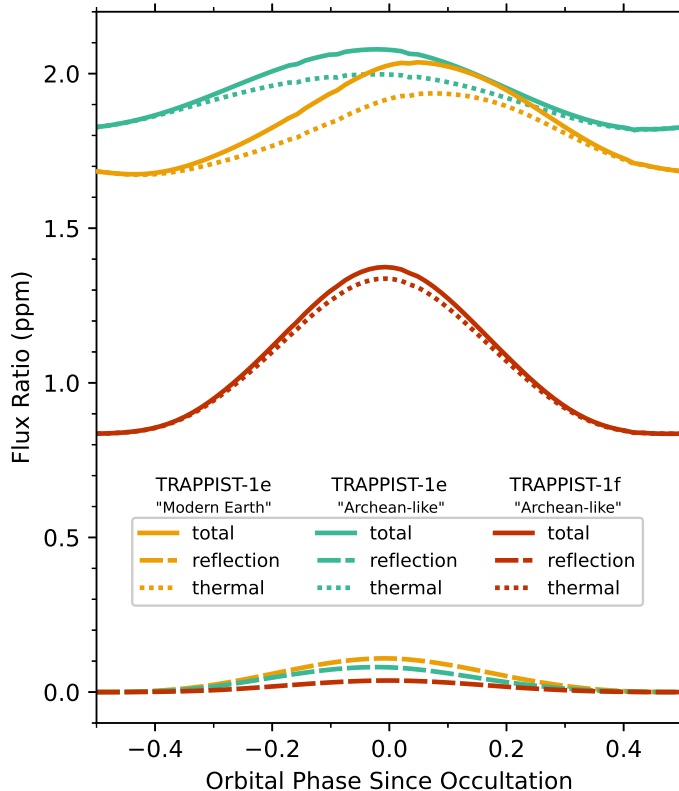


Figure 3. Phase curves of the ROCKE-3D GCM simulations of TRAPPIST-1e with a “modern Earth” atmospheric configuration of 1 bar of N_2 and 400 ppm of CO_2 (yellow), an “Archean-like” model of TRAPPIST-1e with 1bar of N_2 , 10,000 ppm of CO_2 and 2,000 ppm of CH_4 from Charnay et al. (2013) (teal), and a model of TRAPPIST-1f with the same Archean-like atmospheric composition (red). Dashed lines show the reflection components of the phase curves integrated over bandpasses spanning 0.2–20 microns, while the dash-dotted lines show the long-wave thermal components over a wavelength range spanning 3.33–10,000 microns (see Table 2 for the specific spectral resolution). Solid lines show the sum of the reflection and thermal components, i.e. the total outgoing radiation from the top of the atmosphere over a wavelength range of 0.2–10,000 microns. Each curve is phased on the orbital period of the respective planet. Note: In a true photometric observation the transit and occultation events would be present in the phase curves, but are not included here.

bounds in the discrete summations described in this section likely fall somewhere between grid lines, in which case only a fraction of the longitude will be visible to the observer. To correct for this, we create a linearly interpolated function of longitudinal surface luminosity at each point in phase which we use to perform the discrete sums. These surface luminosities are then divided by the stellar luminosity emitted by one hemisphere (integrated over the corresponding short and long-wave bands) to produce flux ratios. Note that the isotropic approximation of the surface luminosity (see Equation 7) does not take into account atmospheric absorption or back-scattering effects.

4.3. Model Phase Curve Discussion

Figure 3 shows the phase curves extracted from the ROCKE-3D GCM simulations for TRAPPIST-1e with the “modern Earth” atmosphere and for TRAPPIST-1e and TRAPPIST-1f with an “Archean-like” atmosphere in both the wide shortwave bandpass spanning 0.2–20 μm , and the wide longwave bandpass spanning 3.33–10,000 μm . The combination of the planet e and f phase variations, phased on the orbit of planet h, are shown in Figure 4. The amplitudes of the phase variations and the effect of their combination are comparable to those predicted in Figure 1 and Table 1, where recall that the albedo was set to unity.

The cause for the differences between the TRAPPIST-1e “modern Earth” phase curves and the “Archean” model phase curves, both in terms of the shift in the

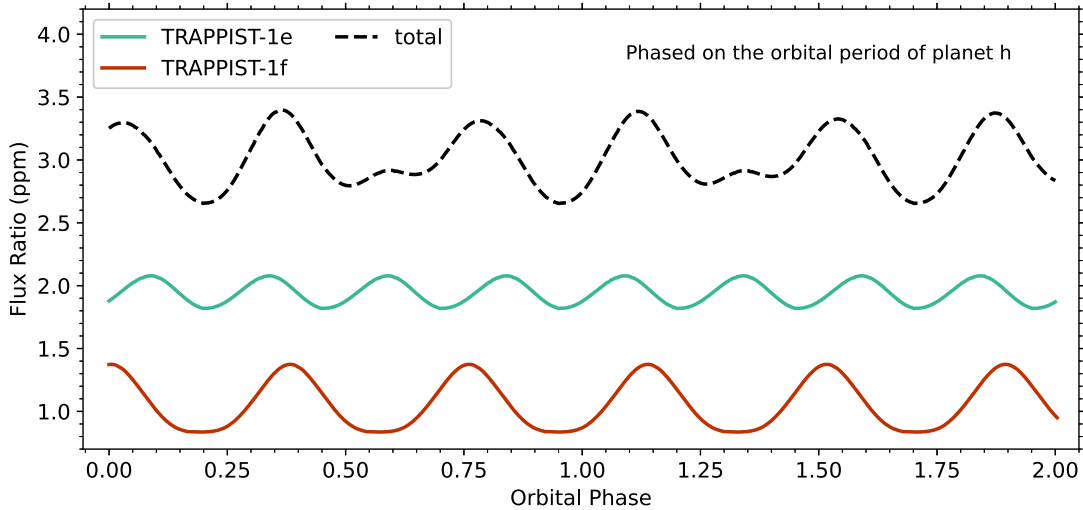


Figure 4. Phase curves of the ROCKE-3D generated models of TRAPPIST-1e (teal) & f (red), both with the atmospheric models of composition B in Charnay et al. (2013). Both curves have been phased on the orbital period of TRAPPIST-1h to showcase how the phase curves of the two planets can interfere (dashed line). Note: In a true photometric observation the transit and occultation events would be present in the phase curves, but are not included here.

peak amplitude and the relative asymmetry, lies in the differences between the distribution of the outgoing radiation across their surfaces. Maps of the outgoing radiation for each model can be examined in the Robinson projections shown in Figure 5. The rows of Figure 5 display the results for the TRAPPIST-1e modern Earth-like atmosphere (top), the TRAPPIST-1e Archean-like atmosphere (middle), and the TRAPPIST-1f Archean-like atmosphere (bottom). The columns are the outgoing short-wave (left) and long-wave (right) radiation from the top of the simulated atmospheres. The sub-stellar point is at the center of each map, where the gray areas in the left column show the sides of the synchronously rotating planets which do not receive stellar radiation. For the long-wave radiation, the westerly-dominant asymmetry about the substellar longitude seen in the “Modern Earth” TRAPPIST-1e map results in a shift of the phase curve maximum of 17° post-occultation, which can be seen in Figure 3. Interestingly, the thermal radiation in the Archean-like model of the same planet extends in the opposite (eastern) direction compared to the model with the more modern Earth-like atmospheric composition, which results in a shift of the phase curve maximum of 7.4° prior to occultation. Likewise, the case of the TRAPPIST-1f long-wave radiation is relatively symmetric around the sub-stellar point (with a slight westward shift of 2.5°), explaining the nearly symmetric phase curve calculated for TRAPPIST-1f shown in Figure 3. It is worth noting that the perturbation of Keplerian orbits detected in

the form of TTVs (Grimm et al. 2018; Agol et al. 2020) will also affect the shift in the peak phase amplitudes. These TTV effects are relatively small, varying the true longitude variations of the planetary orbits by less than $\pm 0.4\%$ of the orbit, compared with with eclipse duration of 0.6% of the orbit.

Figure 6 shows the phase curve amplitudes and shifts of their maxima in each of the wavebands listed in Table 2. Here we can see that the phase shifts of the phase curve maxima and the peak-to-trough amplitudes can vary quite considerably with wavelength. Comparing the phase curves in the shortwave bandpasses (left column) to those in the longwave bandpasses (right column) shows that the shortwave phase curve amplitudes are less than 1 ppm for each TRAPPIST model, and are consistently smaller than the longwave phase curve amplitudes, which can be as high as 25 ppm for the TRAPPIST-1f model (owing to the relatively low thermal redistribution to the nightside). The most promising signal from the models comes from the phase curve of the modern Earth-like TRAPPIST-1e in the farthest infrared waveband, which produces a peak-to-trough amplitude of nearly 7 ppm. Though it has a lower amplitude than the 25 ppm signal produced by the “Archean” TRAPPIST-1f model, the “modern Earth” model of TRAPPIST-1e radiates more photons overall, and, having a shorter orbital period, can be observed over more orbits in the same amount of time. Interestingly, the phase curve maxima in the same FIR band for the TRAPPIST-1e simulations occur 0.30 orbital peri-

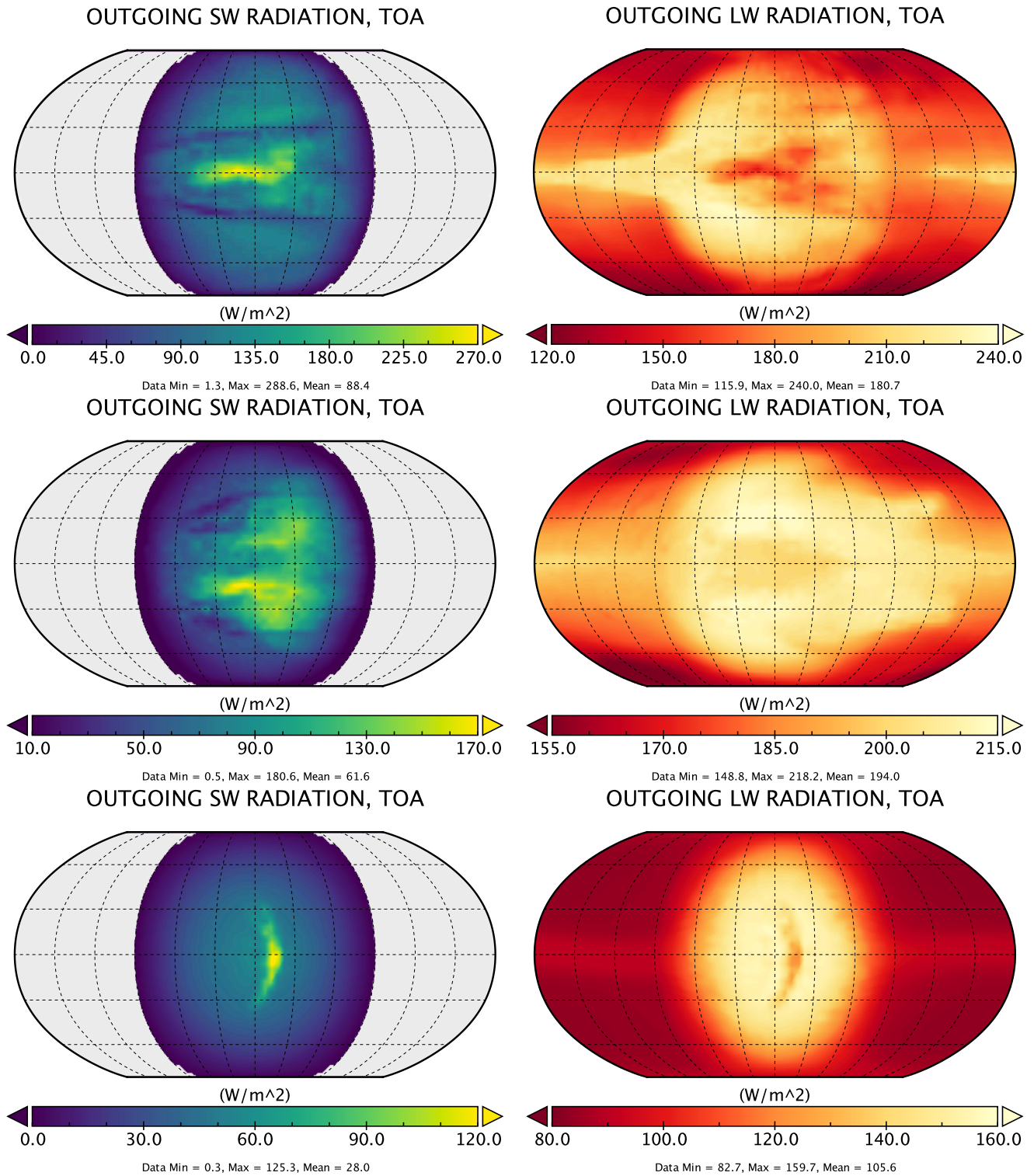


Figure 5. Robinson projections of the outgoing short-wave (left column) and long-wave (right column) radiation from the top of the simulated atmospheres of TRAPPIST-1e & f created by the ROCKE-3D GCM. Each row displays the results of the three simulations explored in this study: the TRAPPIST-1e “modern Earth” atmosphere (top), the TRAPPIST-1e “Archean-like” atmosphere (middle), and the TRAPPIST-1f “Archean-like” atmosphere (bottom). The sub-stellar point is at the center of each map, where the gray areas in the left column show the sides of the synchronously rotating planets which do not receive stellar radiation. Grid lines represent 30° in longitude and latitude. Note that the color in each map is scaled differently to highlight the unique radiation patterns of each surface.

ods post-occultation for the “modern Earth” model and 0.43 orbital periods post-occultation for the “Archean Earth” model, which are caused by a concentration of outgoing radiation from the nightsides of these simulated planets.

5. DISCUSSION

Evaluating the nature of the TRAPPIST-1 planets and their atmospheres remains a continuing focus for much of the exoplanet community (Turbet et al. 2020). Numerous groups have been formed to study the TRAPPIST-1 atmospheres, including an advocacy for robust comparison of atmospheric models (Fauchez et al. 2020). Studies include predictions of potential biosignatures (Hu et al. 2020) and recommendations for their interpretation (Fujii et al. 2018; Schwieterman et al. 2018), and the effects of clouds and hazes in their atmospheres (Moran et al. 2018; Fauchez et al. 2019). Observations of the TRAPPIST-1 system with the James Webb Space Telescope (*JWST*) are discussed in detail by Lustig-Yaeger et al. (2019), whose analysis demonstrates that CO₂-rich atmospheres may be detected with ~ 10 transits, but aerosol hazes, such as the H₂SO₄ haze found on Venus, may limit such detections. The simulations carried out by (Fauchez et al. 2019) further discuss the challenges of detecting H₂O if the planet is not in a moist greenhouse state, thus confining the water vapor to the lower atmosphere.

Several of the TRAPPIST-1 planets lie interior to the HZ in the region defined as the Venus Zone (VZ), described in detail by Kane et al. (2014). GCM models of similar terrestrial planets in high insolation regimes have indicated a rapid atmospheric evolution toward a runaway greenhouse scenario, such as the case of Kepler-1649b (Kane et al. 2018). However, many questions remain regarding the divergence of the apparent Venus–Earth dichotomy and the relative effects of insolation flux, water delivery, and the initial conditions of the interior and atmosphere (Kane et al. 2019). In particular, the potential diversity of terrestrial planets within the TRAPPIST-1 system provide an opportunity to study possible runaway greenhouse environments outside of the nominal VZ through *JWST* observations (Lincowski et al. 2018). Thus, determining evidence of a post-runaway greenhouse environment for the TRAPPIST-1 planets would be extremely insightful for the evolution of terrestrial planets (Lincowski et al. 2019; Way & Del Genio 2020).

A further consideration is that of atmospheric mass loss of the TRAPPIST-1 planets, exacerbated by their relatively old age (Burgasser & Mamajek 2017;

Gonzales et al. 2019) and high XUV environment (Roettenbacher & Kane 2017). For example, the recent discovery of LHS 3844b (Vanderspek et al. 2019) was demonstrated through follow-up observations to have no thick atmosphere (Kreidberg et al. 2019), indicating a volatile-poor formation scenario (Kane et al. 2020). However, the analysis of transmission spectroscopy data performed by Moran et al. (2018) indicates that the outer (d, e, and f) planets may have volatile-rich extended atmospheres. Verification of such extended atmospheres with further observations is critically important for investigating the interplay between atmospheric loss due to stellar erosion and on-going outgassing production of secondary atmospheres (Kite & Barnett 2020).

In Sections 3 and 4, we provide predictions of the phase amplitude due to the reflected light and thermal emission components. Our modeling does not account for the additional effects of Doppler beaming and ellipsoidal variation (Loeb & Gaudi 2003; Zucker et al. 2007). It is unnecessary to account for these aspects of the photometric variations since the planets are terrestrial and will produce negligible beaming and ellipsoidal amplitudes. Specifically, for the TRAPPIST-1 planets, our calculations of the Doppler beaming and ellipsoidal variation amplitudes are 1 and 4 orders of magnitude less than the reflected light amplitude, respectively. For example, in the case of TRAPPIST-1e, the predicted amplitude of the phase variations due to reflected light is 0.835 ppm for the atmosphere model (see Table 1). The corresponding amplitudes of the Doppler beaming and ellipsoidal variations are 0.073 ppm and 0.063 ppb, respectively.

There are several caveats to note with respect to detectability of the phase signatures described here. The differences in the phase signatures between the modern Earth-life and Archean-like atmospheres discussed in Section 4.3 could easily become entangled in the atmospheric signatures, including the effects of cloud distribution and topography, of other planets within the system, each with their own phase signatures. In particular, contamination by the residuals from the inner planets could lead to a similar apparent shift in the phase maxima that was attributed in Section 4.3 to differences in shortwave and longwave radiation. This problem may be partially mitigated through a concerted effort to provide a detailed characterization of the inner planets. The orbital ephemerides of the system is remarkably well established, and the combination of the precisely determined planetary orbits with the phase signatures of the inner planets may allow their effects to be subtracted from

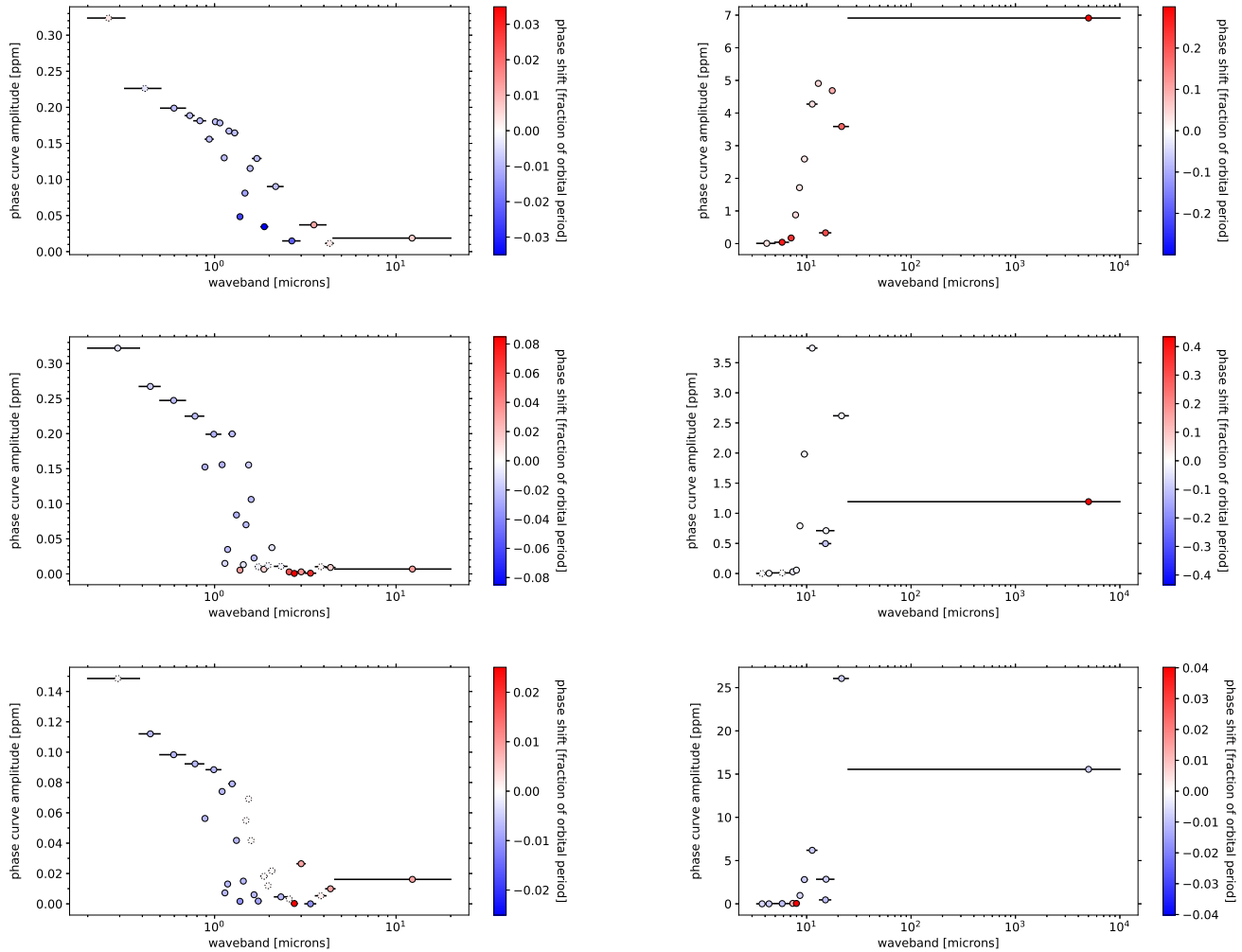


Figure 6. Peak-to-trough phase curve amplitudes for the separate wavebands covered in the ROCKE-3D GCM. Marker locations on the x-axis indicate the central wavelength in each band. Marker colors represent a shift in the phase curve maximum from superior conjunction, where markers with dotted outlines have peak amplitudes that are hidden behind the star during occultation. Redder points indicate a post-occultation maximum while bluer points indicate a pre-occultation maximum. These shifts are caused by a concentration of outgoing radiation on either the eastern hemisphere (blue) or western hemisphere (red) relative to the substellar point. The lefthand column shows the reflected shortwave radiation, while the righthand column shows the outgoing thermal radiation (see Table 2 for the specific bandpasses). The top row shows the modern Earth-like model for TRAPPIST-1e, middle row the Archean Earth-like model for TRAPPIST-1e, and bottom row the Archean Earth-like model for TRAPPIST-1f.

investigations of the phase signatures for planets e and f.

Finally, the detectability of the phase amplitudes presents a significant observational challenge, even if only a single planet were present. For example, Wolf et al. (2019) demonstrated that measurements at the level of ppm, and even ppb, may be required for discerning various aqua-planet scenarios for M dwarf terrestrial planets. Pidhorodetska et al. (2020) provided noise model estimates for a TRAPPIST-1e spectrum, assuming 85 transits observed with future ex-

oplanet facilities. The noise model calculations used the detailed reports for the Habitable Exoplanet Observatory (HabEx) mission (Gaudi et al. 2020), the Large UV/Optical/Infrared Surveyor (LUVOIR) mission (The LUVOIR Team 2019), and the Origins Space Telescope (Meixner et al. 2019). These noise calculations suggest that HabEx, LUVOIR, and Origins achieve a 1σ noise floor at 5 ppm. This noise floor is higher than many of the phase amplitudes predicted in this study for individual planets. Therefore, a more viable goal in the short-term may be to leverage the precisely determined

orbits of the planets to observe the system during the syzygy events of planet-planet occultations, described in Section 3. Such a detection would not easily resolve differences between atmospheres and topographies due to the degeneracies inherent in a multi-planet fit to the data, but would indicate the extent of the scattering and reflective properties of the combined atmospheric profile.

6. CONCLUSIONS

Exoplanetary science has undergone a significant shift in recent years toward detailed characterization of terrestrial planets. This has been enabled by the dramatic rise in discoveries across a broad range of exoplanet demographics, combined with the prolific development of ground- and space-based facilities capable of spectroscopy of planetary atmospheres. Among multi-planet systems, the TRAPPIST-1 system stands out due to its large number of relatively small planets that reside in a range of insolation environments, allowing unprecedented studies of comparative planetology. It is therefore likely that TRAPPIST-1 will be one of the most observed systems with respect to atmospheric characterization studies.

The process of deep characterization of terrestrial exoplanet atmospheres requires significant observing time carried out over multiple wavelength ranges. In addition to the retrieval models applied to spectroscopic data (Barstow et al. 2020), phase variations yield additional insights into atmospheric properties. The amplitude and shape of the variations have a strong wavelength dependence (Sudarsky et al. 2005), also depending on atmospheric composition and topography (Cowan & Agol 2008; Cowan et al. 2013). Furthermore, the seasonal variations that may correspond with photometric variability can serve as a biosignature (Olson et al. 2018). Thus, the detection of phase variations for a system with the astrobiological significance of TRAPPIST-1 would add complementary information to the overall characterization of the planets. Even so, the relatively low signal-to-noise phase signals expected in the face of stellar ac-

tivity present significant challenges in the years ahead, motivating additional effort to distinguish between planetary and stellar photometric variability (Serrano et al. 2018).

In terms of detectable signatures, our simulations show that the observational prospects of detecting the combined phase amplitude of several TRAPPIST-1 planets with *JWST*, though feasible, will likely provide limited resolution of the phase change with respect to the orbital period. A detailed observing campaign that could robustly use the signatures presented here to distinguish between, for example, the Archean-like and modern Earth-like scenarios described in Section 4, will need to filter out the phase signature from other planets within the system and also overcome the noise floor limitations of missions such as HabEx, LUVOIR, and Origins. However, the prospect of such deep insights into the atmospheric and surface characteristics of the the TRAPPIST-1 planets motivates further increasing atmospheric characterization capabilities in the coming years.

ACKNOWLEDGEMENTS

The authors would like to thank the anonymous referee for the constructive feedback on the manuscript, and Eric T. Wolf for his guidance regarding ROCKE-3D and SOCRATES. This research has made use of the NASA Exoplanet Archive, which is operated by the California Institute of Technology, under contract with the National Aeronautics and Space Administration under the Exoplanet Exploration Program. The results reported herein benefited from collaborations and/or information exchange within NASA’s Nexus for Exoplanet System Science (NExSS) research coordination network sponsored by NASA’s Science Mission Directorate. This material is based upon work supported by the National Science Foundation under Grant No. DGE-1644869.

Software: ROCKE-3D (Way et al. 2017), Panoply, astropy

REFERENCES

- Agol, E., Dorn, C., Grimm, S. L., et al. 2020, arXiv e-prints, arXiv:2010.01074
- Angerhausen, D., DeLarme, E., & Morse, J. A. 2015, *PASP*, 127, 1113
- Baraffe, I., Homeier, D., Allard, F., & Chabrier, G. 2015, *A&A*, 577, A42
- Barstow, J. K., Changeat, Q., Garland, R., et al. 2020, *MNRAS*, 493, 4884
- Becker, J., Gallo, E., Hodges-Kluck, E., Adams, F. C., & Barnes, R. 2020, *AJ*, 159, 275
- Bolmont, E., Selsis, F., Owen, J. E., et al. 2017, *MNRAS*, 464, 3728
- Burgasser, A. J., & Mamajek, E. E. 2017, *ApJ*, 845, 110
- Charnay, B., Forget, F., Wordsworth, R., et al. 2013, *Journal of Geophysical Research (Atmospheres)*, 118, 10,414

- Cowan, N. B., & Agol, E. 2008, *ApJL*, 678, L129
- Cowan, N. B., Fuentes, P. A., & Haggard, H. M. 2013, *MNRAS*, 434, 2465
- de Wit, J., Wakeford, H. R., Lewis, N. K., et al. 2018, *Nature Astronomy*, 2, 214
- Ducrot, E., Sestovic, M., Morris, B. M., et al. 2018, *AJ*, 156, 218
- Edwards, J. M. 1996, *Journal of Atmospheric Sciences*, 53, 1921
- Edwards, J. M., & Slingo, A. 1996, *Quarterly Journal of the Royal Meteorological Society*, 122, 689
- Esteves, L. J., De Mooij, E. J. W., & Jayawardhana, R. 2013, *ApJ*, 772, 51
- . 2015, *ApJ*, 804, 150
- Faucher, T. J., Turbet, M., Villanueva, G. L., et al. 2019, *ApJ*, 887, 194
- Faucher, T. J., Turbet, M., Wolf, E. T., et al. 2020, *Geoscientific Model Development*, 13, 707
- Fleming, D. P., Barnes, R., Luger, R., & VanderPlas, J. T. 2020, *ApJ*, 891, 155
- Fujii, Y., Angerhausen, D., Deitrick, R., et al. 2018, *Astrobiology*, 18, 739
- Gaia Collaboration, Brown, A. G. A., Vallenari, A., et al. 2018, *A&A*, 616, A1
- Gaudi, B. S., Seager, S., Mennesson, B., et al. 2020, arXiv e-prints, arXiv:2001.06683
- Gelino, D. M., & Kane, S. R. 2014, *ApJ*, 787, 105
- Gillon, M., Jehin, E., Lederer, S. M., et al. 2016, *Nature*, 533, 221
- Gillon, M., Triaud, A. H. M. J., Demory, B.-O., et al. 2017, *Nature*, 542, 456
- Gonzales, E. C., Faherty, J. K., Gagné, J., et al. 2019, *ApJ*, 886, 131
- Grimm, S. L., Demory, B.-O., Gillon, M., et al. 2018, *A&A*, 613, A68
- Hilton, J. L. 1992, *Explanatory Supplement to the Astronomical Almanac*, ed. Seidelmann, P.K. (University Science Books, Mill Valley CA), p. 383
- Hori, Y., & Ogihara, M. 2020, *ApJ*, 889, 77
- Hu, R., Demory, B.-O., Seager, S., Lewis, N., & Showman, A. P. 2015, *ApJ*, 802, 51
- Hu, R., Peterson, L., & Wolf, E. T. 2020, *ApJ*, 888, 122
- Jansen, T., & Kipping, D. 2018, *MNRAS*, 478, 3025
- . 2020, *MNRAS*, 494, 4077
- Kane, S. R. 2018, *ApJL*, 861, L21
- Kane, S. R., Ceja, A. Y., Way, M. J., & Quintana, E. V. 2018, *ApJ*, 869, 46
- Kane, S. R., & Gelino, D. M. 2010, *ApJ*, 724, 818
- . 2011, *ApJ*, 729, 74
- . 2012, *MNRAS*, 424, 779
- . 2013, *ApJ*, 762, 129
- Kane, S. R., Gelino, D. M., Ciardi, D. R., Dragomir, D., & von Braun, K. 2011, *ApJ*, 740, 61
- Kane, S. R., Kopparapu, R. K., & Domagal-Goldman, S. D. 2014, *ApJL*, 794, L5
- Kane, S. R., Roettenbacher, R. M., Unterborn, C. T., Foley, B. J., & Hill, M. L. 2020, *The Planetary Science Journal*, 1, 36
- Kane, S. R., Hill, M. L., Kasting, J. F., et al. 2016, *ApJ*, 830, 1
- Kane, S. R., Arney, G., Crisp, D., et al. 2019, *Journal of Geophysical Research (Planets)*, 124, 2015
- Kite, E. S., & Barnett, M. N. 2020, *Proceedings of the National Academy of Science*, 117, 18264
- Kreidberg, L., Koll, D. D. B., Morley, C., et al. 2019, *Nature*, 573, 87
- Lincowski, A. P., Lustig-Yaeger, J., & Meadows, V. S. 2019, *AJ*, 158, 26
- Lincowski, A. P., Meadows, V. S., Crisp, D., et al. 2018, *ApJ*, 867, 76
- Loeb, A., & Gaudi, B. S. 2003, *ApJL*, 588, L117
- Luger, R., Lustig-Yaeger, J., & Agol, E. 2017a, *ApJ*, 851, 94
- Luger, R., Sestovic, M., Kruse, E., et al. 2017b, *Nature Astronomy*, 1, 0129
- Lustig-Yaeger, J., Meadows, V. S., & Lincowski, A. P. 2019, *AJ*, 158, 27
- Madden, J. H., & Kaltenecker, L. 2018, *Astrobiology*, 18, 1559
- Mansfield, M., Kite, E. S., Hu, R., et al. 2019, *ApJ*, 886, 141
- Meixner, M., Cooray, A., Leisawitz, D., et al. 2019, arXiv e-prints, arXiv:1912.06213
- Moran, S. E., Hörst, S. M., Batalha, N. E., Lewis, N. K., & Wakeford, H. R. 2018, *AJ*, 156, 252
- Olson, S. L., Schwieterman, E. W., Reinhard, C. T., et al. 2018, *ApJL*, 858, L14
- Peacock, S., Barman, T., Shkolnik, E. L., Hauschildt, P. H., & Baron, E. 2019, *ApJ*, 871, 235
- Pidhorodetska, D., Faucher, T. J., Villanueva, G. L., Domagal-Goldman, S. D., & Kopparapu, R. K. 2020, *ApJL*, 898, L33
- Quintana, E. V., Rowe, J. F., Barclay, T., et al. 2013, *ApJ*, 767, 137
- Roettenbacher, R. M., & Kane, S. R. 2017, *ApJ*, 851, 77
- Schwieterman, E. W., Kiang, N. Y., Parenteau, M. N., et al. 2018, *Astrobiology*, 18, 663
- Selsis, F., Wordsworth, R. D., & Forget, F. 2011, *A&A*, 532, A1
- Serrano, L. M., Barros, S. C. C., Oshagh, M., et al. 2018, *A&A*, 611, A8
- Shporer, A. 2017, *PASP*, 129, 072001

- Shporer, A., Wong, I., Huang, C. X., et al. 2019, *AJ*, 157, 178
- Sudarsky, D., Burrows, A., Hubeny, I., & Li, A. 2005, *ApJ*, 627, 520
- The LUVOIR Team. 2019, arXiv e-prints, arXiv:1912.06219
- Turbet, M., Bolmont, E., Bourrier, V., et al. 2020, *SSRv*, 216, 100
- Unterborn, C. T., Desch, S. J., Hinkel, N. R., & Lorenzo, A. 2018, *Nature Astronomy*, 2, 297
- Vanderspek, R., Huang, C. X., Vanderburg, A., et al. 2019, *ApJL*, 871, L24
- Way, M. J., & Del Genio, A. D. 2020, *Journal of Geophysical Research (Planets)*, 125, e06276
- Way, M. J., Aleinov, I., Amundsen, D. S., et al. 2017, *ApJS*, 231, 12
- Wheatley, P. J., Louden, T., Bourrier, V., Ehrenreich, D., & Gillon, M. 2017, *MNRAS*, 465, L74
- Wolf, E. T. 2017, *ApJL*, 839, L1
- Wolf, E. T., Kopparapu, R. K., & Haqq-Misra, J. 2019, *ApJ*, 877, 35
- Wong, I., Benneke, B., Shporer, A., et al. 2020, *AJ*, 159, 104
- Zhang, Z., Zhou, Y., Rackham, B. V., & Apai, D. 2018, *AJ*, 156, 178
- Zucker, S., Mazeh, T., & Alexander, T. 2007, *ApJ*, 670, 1326